Nanoscale

ROYAL SOCIETY OF CHEMISTRY

COMMUNICATION

View Article Online
View Journal | View Issue

Cite this: *Nanoscale*, 2025, **17**, 14630

Received 21st February 2025,
Accepted 22nd May 2025

DOI: 10.1039/d5nr00785b

rsc.li/nanoscale

A biomimetic Fe(III)–metal–organic framework nanosphere-based dual modal probe for aqueous and intracellular sensing of nicotine and its metabolite cotinine†

Arshminder Kaur Dhillon,[a] Agrim Jhilta,[a] Ritu Ladhi,[a] Harshita Bagdwal,[a] Ashi Singh,[b] Rahul K. Verma [a] and Monika Singh *[a]

Integration of novel biocompatible nanostructures as effective sensing platforms is still of great significance for robust and rapid analysis. Herein, novel iron(III) metal–organic framework (Fe-MOF) nanospheres with the formula $[Fe_3(\mu_3\text{-}O)(C_7O_2H_5)_6(COO)_2(H_2O)\cdot 2DMF]$ were successfully developed and characterized by single crystal X-ray diffraction (SXRD) studies. Interestingly, fluorescence studies reveal that Fe-MOF is an effective multi-functional turn-on sensor for nicotine and cotinine that exhibits a blue shift, a low detection limit, notable recyclability, and good anti-interference ability. This material satisfies essential biological criteria by being minimally toxic to living cells (L929 and A549 cell lines) and retaining structural stability in water across a broad pH range (3–11), enabling its successful application in biological imaging of nicotine and cotinine in living cells. To our knowledge, this is the first report of fluorescence enhancement for cotinine detection with a metal–organic framework. Density functional theory (DFT) calculations and ultraviolet-visible (UV-vis) absorption studies have elucidated the plausible sensing mechanism. This study significantly expands the potential of Fe-MOF in sensing and biological applications.

Introduction

Smoking is a pervasive public issue with significant health ramifications, contributing to over 3 million deaths globally every year.[1] Additionally, exposure to second-hand smoke has profound health implications for non-smokers, particularly affecting children and pregnant women.[2] Tobacco smoke comprises a diverse array of over 7000 harmful chemical compounds, among which nicotine is the primary active ingredient, which is a psychoactive and highly addictive alkaloid.[3,4] In adults, a lethal dose of nicotine is considered to be between 0.5 and 1.0 mg kg^{-1} of body weight.[5,6] Nicotine induces tachycardia and hypertension. It is associated with cardiovascular diseases, respiratory distress, and neoplastic conditions.[7,8] Nicotine aggravates the progression of lung cancer by stimulating the growth of pre-existing cancer cells.[9]

Cotinine, on the other hand, is nicotine's primary metabolite, produced by the kidney, liver, and lungs, and serves as a robust biomarker for detecting smoking. It persists in blood, saliva, and urine.[10] Detecting nicotine and cotinine in cells is pivotal for advancing scientific understanding across various disciplines, from fundamental cellular research to translational studies to improve human health and well-being.[1] To advance public health objectives, it is critical to develop sensitive, selective, and economically viable sensors that accurately detect nicotine and its metabolite, cotinine.

Techniques like high-performance liquid chromatography, capillary electrophoresis, radioimmunoassay, electrochemical assays, and gas chromatography-mass spectrometry are commonly employed for nicotine and cotinine detection.[11,12] However, these methods are often constrained by their time-consuming nature, the requirement for expensive analytical instruments, prolonged sample purification processes, a limited detection range, and the need for skilled technical personnel.[13,14] In contrast, fluorometric detection techniques offer quick response, signal visualization, cost-efficiency, and accelerated data acquisition.[15]

Metal–organic frameworks (MOFs) offer unique advantages by integrating dual functions like metal nodes and linkers into a single entity.[16] Their application in sensing ions, small molecules, and hazardous compounds is particularly promising due to intricate nanocavities with highly ordered recognition sites, structural diversity, and host–guest complexation capabilities, enabling rapid response mechanisms.[17–19] Furthermore, the heterogeneous nature of MOFs with good thermal and solvent stability facilitates easy recovery.[20,21]

MOFs have been extensively studied for detecting a wide range of analytes. However, there are limited reports on their

[a]*Institute of Nano Science and Technology, Knowledge City, Sector-81, Mohali-140306, Punjab, India. E-mail: monika@insta.ac.in*
[b]*Department of Chemistry, Indian Institute of Technology, Delhi, India*

†Electronic supplementary information (ESI) available. CCDC 2303436. For ESI and crystallographic data in CIF or other electronic format see DOI: https://doi.org/10.1039/d5nr00785b

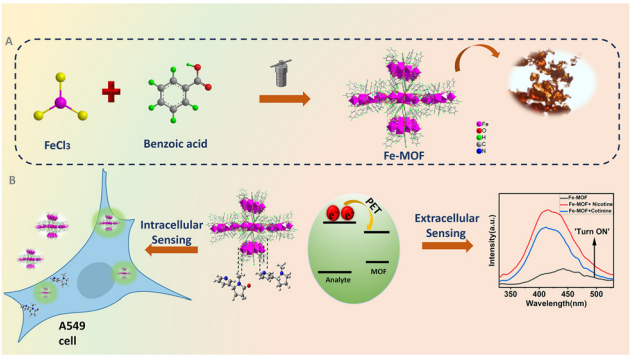

Scheme 1 Schematic illustration of the preparation of Fe-MOF and its application in sensing.

use for nicotine detection and no prior reports of their use as fluorometric 'turn-on' sensors for cotinine. Among the various MOFs, iron (Fe)-based MOFs are of particular interest due to the abundance of iron on Earth, making them less toxic to living cells and highly attractive for diverse applications.[22] For instance, Jia and co-workers have synthesized an Fe(III)-based MOF with benzene dicarboxylic acid linkers, exhibiting pronounced fluorescence enhancement upon interaction with $MeHg^+$, underscoring its suitability as a fluorescent sensing platform.[23] Also, Xie *et al.* used Fe–metal–organic framework nanooctahedra as a 'turn-on' sensor for the detection of arsenate.[24]

Herein, we synthesized Fe-MOF nanospheres *via* a solvothermal method using $FeCl_3$ and benzoic acid in DMF and acetonitrile (Scheme 1A). The structural characteristics of the synthesized material were systematically examined using various techniques.

To demonstrate its functional applications, the sensing behaviour of the synthesized material is explored for nicotine and cotinine detection, including evaluation of their selectivity in the presence of other competing ions in saliva and urine, recyclability, and limit of detection. Fe-MOF exhibits remarkable 'turn-on' fluorescence for nicotine and cotinine. In addition, cell viability and sensing applications in living cells were investigated, along with a study of the plausible mechanistic insights underlying nicotine and cotinine detection using Fe-MOF (Scheme 1B). It represents the first instance where Fe-MOF demonstrates the capability to detect nicotine and cotinine in living cells, providing distinct advantages for ongoing research.

Experimental

Materials

Potassium chloride (KCl) was obtained from Central Drug House (P) Ltd. Urea, glucose, and sodium bicarbonate ($NaHCO_3$) were purchased from Tokyo Chemical Industry (India) Pvt. Ltd. α-Amylase was purchased from Sisco Research Laboratories Pvt. Ltd (SRL), India. Lysozyme, creatinine, sodium chloride (NaCl), magnesium chloride ($MgCl_2$), calcium chloride ($CaCl_2$), iron(III) chloride anhydrous, dimethylformamide, and acetonitrile were purchased from Sigma Aldrich Chemicals Private Limited. For the cell culture experimental study, Dulbecco's modified Eagle's medium (DMEM) with low glutamine (DMEM), Kaighn's Modification of Ham's F-12 Medium (F12/K), phosphate buffered saline (PBS), and trypsin-EDTA solution (1×) were obtained from Himedia India. Fetal bovine serum (FBS) and antibiotic–antimycotic (100×) were obtained from GIBCO (USA). L929 fibroblast cells and A549 lung cancer cells were procured from the National Centre for Cell Science (NCCS), Pune.

Results and discussion

Structural and morphological characterization of Fe-MOF

Single-crystal X-ray diffraction (SXRD) studies elucidated that Fe-MOF exhibited a 3-dimensional architectural framework. The compound $[Fe_3(\mu_3\text{-}O)(C_7O_2H_5)_6(COO)_2(H_2O)\cdot 2DMF]$ crystallizes in the orthorhombic crystal system and *Pbca* space group. As shown in Fig. 1a, the asymmetric unit comprises three types of Fe ions, six benzoic acid (BA) ligands, one formate ion (formed by decomposition of DMF through hydrolysis), two free DMF molecules, and one water molecule. Table S1 in the ESI† summarizes the crystal and refinement data.

The structure consists of an oxo-centered trinuclear Fe cluster, interconnected by the carboxylate oxygen of benzoic acid. Fe2 is in a hexacoordinated environment surrounded by four O atoms of the carboxylate BA ligand and a terminal aqua ligand. Similarly, Fe1 and Fe3 are octahedrally coordinated with four O atoms of the carboxylate of the BA ligand and one formate ion. The less hindered formate group acts as a bridging agent between two Fe ions, resulting in a continuous

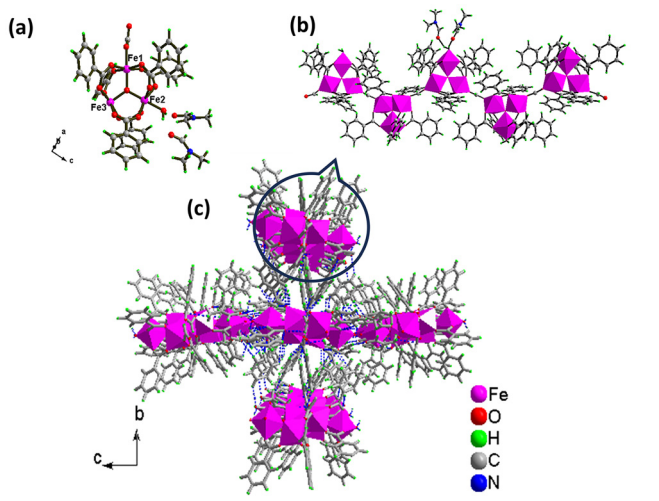

Fig. 1 (a) Coordination environment of Fe ions in Fe-MOF. (b) The 1D chain-like structure of Fe-MOF. (c) The 3D framework structure of Fe-MOF.

linkage of Fe–formate–Fe, which forms 1D chains. These chains are further expanded into the 3D framework through hydrogen bonding (Fig. 1b and c). The total potential solvent-accessible volume for Fe-MOF, calculated using PLANTON, is 2140.1 Å^3 (21.7%) per unit cell.

The homogeneity and phase purity of the material were confirmed by powder X-ray diffraction. As revealed in Fig. S2,† the well-defined crystal structure and main diffraction peaks match the simulation pattern of Fe-MOF well. Thermogravimetric analysis (TGA) was performed under a nitrogen atmosphere from 22 to 800 °C with a 20 °C min^{-1} heating rate. The first weight loss of 5.7 wt% from 25 to 160 °C may be due to the elimination of coordinated water molecules.[25] As temperature increases, the framework starts to collapse at 390 °C, indicating good thermal stability (Fig. S3†).

The particle size and morphology of the synthesized Fe-MOF were initially determined using FESEM imaging. Most of the Fe-MOF particles exhibit good dispersity and a typical nano-spherical morphology, as shown in Fig. 2a. Furthermore, we verified the elemental composition of Fe-MOF, through energy dispersive X-ray spectroscopy (EDX) mapping (Fig. 2c), which shows that iron (pink zone), carbon (green zone), oxygen (red zone), and nitrogen (yellow zone) elements are homogeneously distributed throughout the nonspherical frameworks, with Fe making up 1.8 atomic percent. TEM characterization confirmed the well-defined spherical morphology, as shown in Fig. 2b, consistent with the FESEM results. The textural properties of the synthesized Fe-MOF were examined using nitrogen adsorption–desorption isotherms. The Braeuer–Emmett–Teller (BET) surface area was found to be 15.932 m^2 g^{-1}, with an average pore size of approximately 7.33 nm, and the pore volume was 0.040 cm^3 g^{-1} (Fig. S4a and S4b†).

The FT-IR spectra (Fig. S5†) confirmed the presence of key functional groups in Fe-MOF. The bands observed at around 3700–3231 cm^{-1} correspond to the stretching vibrations of the O–H groups from H_2O molecules.[26] Peaks in the regions of 1666–1661cm^{-1} and 1566–1408 cm^{-1} are attributed to the asymmetric and symmetric stretching vibrations of the COO^- group, respectively.[27] A band at 1105 cm^{-1} indicates in-plane C–C stretching, while bands at around 718 cm^{-1} correspond to the out-of-plane stretching vibrations of C–H aromatic groups.[28] Additionally, a noticeable peak centered at around 549 cm^{-1} is ascribed to Fe–O vibrational modes.[29]

X-ray photoelectron spectroscopy (XPS) was performed to determine the chemical composition and elemental valence states of Fe-MOF. The survey scan confirms the presence of Fe, N, C, and O (Fig. S6a†). The high-resolution XPS spectra of Fe2p could be split into Fe $2p_{1/2}$ (724.1 eV) and $2p_{3/2}$ (710.6 eV).[30] The distance between these two peaks is about 13.9 eV, which agrees with the presence of Fe^{3+}. Meanwhile, the peaks corresponding to the shakeup satellites of Fe(III) at 714.28 eV and 727.58 eV are easily observed. The O1s peak was deconvoluted into three components at 532.9 eV, 532.1 eV, and 531.7 eV, attributed to O–C=O, O–H groups, and Fe–O, respectively.[31,32] The C1s spectrum shows peaks at 284.9 eV, 288.7 eV, and 286.0 eV, corresponding to C=C/C–C, O–C=O, and C–N groups, respectively.[33,34] The N1s spectrum displays a peak at 399.6 eV, assignable to the C–N group (Fig. S6†).[33]

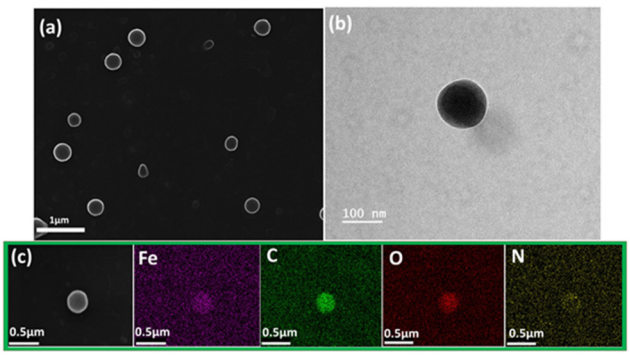

Fig. 2 (a) FESEM and (b) TEM images of Fe-MOF nanospheres. (c) Elemental mapping of Fe, C, O, and N, respectively.

Optical properties of Fe-MOF

Diffuse reflectance (DR) measurements (Fig. S7b†) of the solid-state powder of Fe-MOF are conducted, showing that the absorption bands near 230 nm can be attributed to the π–π* transition of the ligand and the band in the region of 350 nm–400 nm can be attributed to the presence of LMCT transitions.[35–37] BA and Fe-MOF emission spectra were examined at room temperature, with an excitation wavelength of 300 nm (Fig. S7a†). The free BA ligand shows an emission peak at 400 nm. The emission peak of Fe-MOF was red-shifted relative to the ligand emission due to the coordination interaction between the ligand and metal within the framework.[38] To confirm the reliability of Fe-MOF as a fluorescent probe, an assessment of its fluorescent stability in an aqueous solution was conducted by monitoring emission spectra over 96 hours (Fig. S8†). The results revealed no significant decrease in fluorescence, indicating excellent storage stability.

The aqueous-phase stability of Fe-MOF was further evaluated by immersing the sample in water for 48 hours, followed by PXRD analysis. As depicted in Fig. S9,† the crystalline structure remained intact, demonstrating superior water tolerance, making it a promising candidate for real-world applications. Additionally, the acid–base stability of Fe-MOF was examined, an essential factor for physiological applications. The PXRD pattern was recorded after immersing the material in an aqueous solution with pH levels ranging from 3 to 11 for 18 hours (Fig. S10b†) and structural stability was evaluated under these conditions. The effect of pH on the fluorescence intensity of the Fe-MOF suspension was also examined. As shown in Fig. S10a,† the fluorescence intensity remained almost stable across a wide pH range of 3 to 11, highlighting the probe's robustness against pH variations.

Fluorescence sensing of nicotine and cotinine using Fe-MOF

For fluorescence studies, Fe-MOF was dispersed in water through ultrasonication for one hour to achieve a uniform suspension. To elucidate the sensing capabilities of Fe-MOF in an aqueous medium for nicotine, fluorescence titration experiments were conducted with incremental addition of nicotine (2.5 to 35 μM of a 5 mM solution). Notably, as shown in Fig. 3a, Fe-MOF exhibits a significant turn-on effect in luminescence intensity upon adding nicotine (λ_{ex} = 300 nm and λ_{em} = 440 nm). Also, images under a UV lamp are shown in Fig. S16(c).† Furthermore, to evaluate the selectivity and anti-interference properties of Fe-MOF towards nicotine, common saliva components ($CaCl_2$, NaCl, α-amylase, lysozyme, $MgCl_2$, KCl, and $NaHCO_3$) were tested. As illustrated in Fig. S11a,† the luminescence intensity of Fe-MOF showed a substantial increase upon interaction with nicotine compared to the baseline, whereas the presence of other analytes had minimal impact on its luminescence.

Similarly, Fe-MOF exhibited a turn-on effect upon adding cotinine (2.5 to 35 μM of 5 mM solution), as shown in Fig. 3c. These findings unequivocally established Fe-MOF as an ideal fluorescence sensor. Cotinine levels in urine are typically 4–6 times higher than in other parts of the body, and they serve as prominent biomarkers. In a parallel manner, the interference of major urine components (creatinine, glucose, KCl, NaCl, and urea) was examined to advance the potential of Fe-MOF for detecting cotinine in the urine environment. As shown in Fig. S11b,† other components had no significant effect on the emission spectra. A comparative analysis of emission intensities confirmed that these substances do not interfere with the cotinine detection in urine.

The sensitivity of Fe-MOF for nicotine and cotinine was further validated by measuring the LOD using the equation $3\sigma/m$ (where σ represents the standard deviation of five consecutive intensity measurements of the blank sample in the absence of the analyte, and m is the slope of the concentration *vs.* intensity graph).[39] The LOD values were calculated to be 0.94 μM and 1.7 μM for nicotine and cotinine, respectively. The emission peak also displayed a blue shift with the enhancement of fluorescence intensity, exemplifying the proficient sensing efficacy of nicotine and cotinine. The fluorometric turn-on detection of nicotine has been scarcely addressed in the literature. To our knowledge, there are no prior reports on using an MOF as a fluorometric turn-on sensor for cotinine.

Framework stability and recyclability. To assess the multicyclic detection capability of Fe-MOF, the material was retrieved after each experiment through centrifugation, rinsed with distilled water, and air-dried. The recovered Fe-MOF consistently showed nearly identical fluorescence enhancement across five sensing-recovery cycles (Fig. 3e and f), indicating that it can be reused without any loss in sensing performance.

Plausible mechanism

Relational experiments were conducted to elucidate the mechanism by which Fe-MOF functions as a sensor for nicotine and cotinine. Firstly, the corresponding PXRD pattern demonstrates that the Fe-MOF structure remains intact after sensing nicotine and cotinine, indicating that framework collapse is not the driving mechanism of the sensing process[40] (Fig. 4a). The fluorescence sensing of Fe-MOF for nicotine and cotinine is a dynamic process, as indicated by an increase in the fluorescence lifetime of Fe-MOF after detecting nicotine and cotinine (Fig. S12 and Table S2†).[41] The UV-*vis* absorption spectra of Fe-MOF dispersed in an aqueous medium in the presence of nicotine and cotinine were also examined (Fig. S16†). The absorption spectra exhibited a significant enhancement and a slight blue shift with the addition of analytes, suggesting that enhancement may be caused by host–guest interactions.[42]

To further investigate the mechanism driving the 'turn-on' fluorescence, we combined DFT calculations at the B3LYP/6-31G level with experimental data. The computational analysis identified the energy levels of the highest occupied molecular orbital (HOMO) and the lowest unoccupied molecular orbital (LUMO) of nicotine and cotinine.[43] The energy levels of the LUMO and HOMO of Fe-MOF were determined using the first redox potentials from cyclic voltammetry and solid-state UV-vis

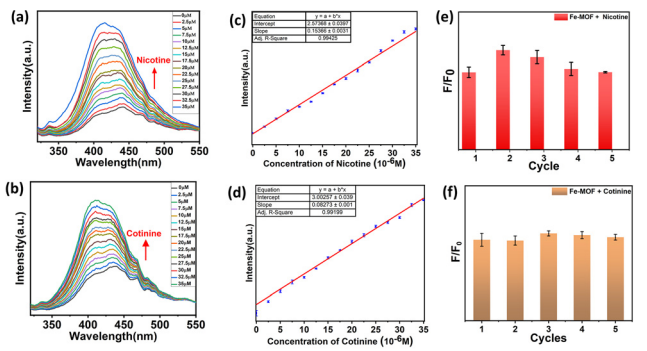

Fig. 3 Emission spectra of Fe-MOF upon addition of different concentrations of nicotine (a) and cotinine (c), and the corresponding linear fitting relationship between nicotine (b) and cotinine (d) concentrations and Fe-MOF fluorescence intensity. Fluorescence intensity of Fe-MOF in sensing nicotine (e) and cotinine (f) for five cycles. (error bars in c–f indicate the deviation of three repetitive measurements).

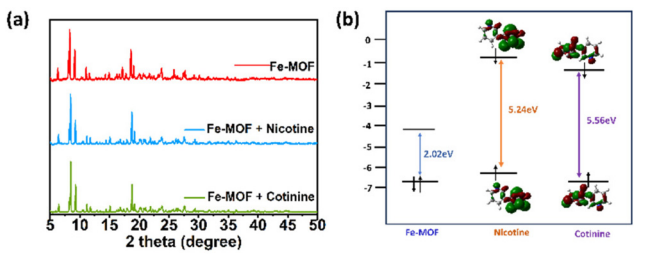

Fig. 4 (a) PXRD pattern of Fe-MOF before and after sensing nicotine and cotinine and (b) energy level diagram of Fe-MOF, nicotine, and cotinine.

reflectance band measurements (Fig. S13 and S14†).[44] The results elucidated that the LUMO level of Fe-MOF (−4.5 eV) is lower than those of nicotine (−0.9 eV) and cotinine (−1.2 eV) (Fig. 4b). A significant energy gap was observed between the LUMO levels of Fe-MOF and the analytes, indicating a favorable thermodynamic driving force for electron transfer from the analytes to Fe-MOF.[42,45] For electron-rich analytes, excited electrons transfer from the analyte's LUMO to that of the MOF, enhancing the fluorescence. Consequently, upon photoexcitation, the electrons may be transferred from the LUMO of the analytes to the LUMO of the MOF, resulting in an increased electron population and enhanced fluorescence[27]

Biocompatibility and cellular internalization of Fe-MOF

Based on the observed results, a novel Fe-MOF was further investigated for its potential in advancing biological imaging applications. To evaluate its cytotoxicity and assess its suitability for such applications, Fe-MOF was tested using the MTT assay on A549 (human lung cancer) cells over a range of concentrations from 5 to 200 μg mL^{-1}. After 24 hours of incubation, the cell viability was measured. As shown in Fig. 5b, the results indicated that A549 cells maintained over 85% viability even at the highest concentration of 200 μg mL^{-1}. This suggests that Fe-MOF exhibited minimal cytotoxicity at these concentrations and supports its biocompatibility for further investigation in biological imaging. Similarly, the cytotoxicity

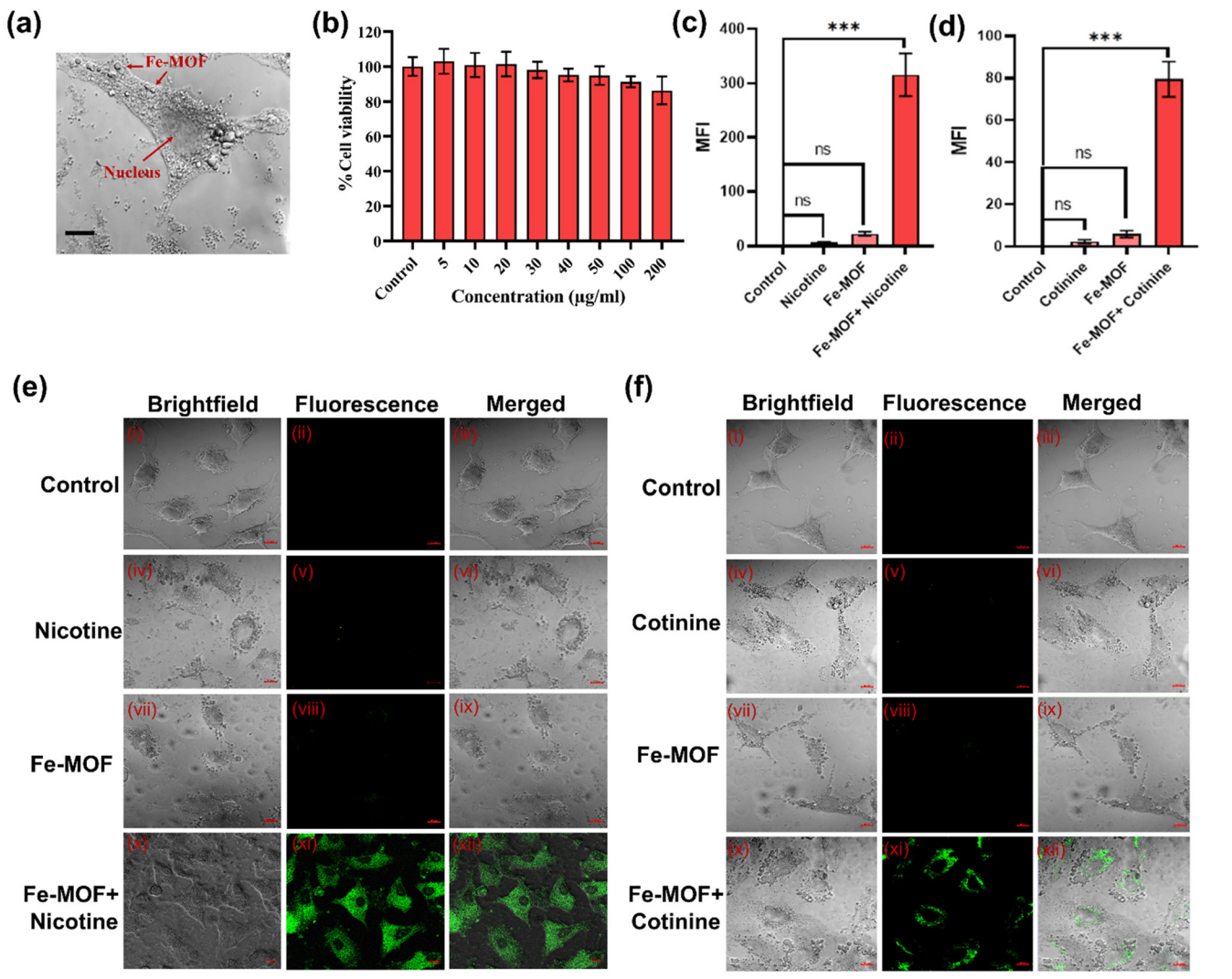

Fig. 5 (a) Cellular uptake and intracellular distribution of Fe-MOF in A549 cells (scale bar = 2 μm) and (b) cytotoxicity assay of A549 cell lines treated with different concentrations of Fe-MOF (red bar). (c and d) Comparative analysis of mean fluorescence intensity of Fe-MOF alone and Fe-MOF combined with nicotine and cotinine, respectively, measured *via* CLSM (*P < 0.05; **P < 0.01; ***P < 0.001; ns). (e) (iv, vii and x) Bright-field transmission images of nicotine, Fe-MOF, and Fe-MOF with nicotine (25 μM). (e) (v, viii and xi) Fluorescence bright-field images of nicotine, Fe-MOF, and Fe-MOF with nicotine. (e) (vi, ix and xi) Merged images of nicotine, Fe-MOF, and Fe-MOF with nicotine (scale bar = 10 μm). (f) (iv, vii and x) bright-field transmission images of cotinine, Fe-MOF, and Fe-MOF with cotinine (25 μM). (f) (v, viii and xi) Fluorescence bright-field images of cotinine, Fe-MOF, and Fe-MOF with cotinine. (f) (vi, ix and xii) Merged images of cotinine, Fe-MOF, and Fe-MOF with cotinine.

of Fe-MOF was evaluated on normal fibroblast L929 cells using the MTT assay. As shown in Figure S17,† L929 cells treated with Fe-MOF at 200 μg mL^{-1} maintained 78% viability after 24 hours.

This further confirms that Fe-MOF exhibited minimal cytotoxic effects across different cell types, with no significant drop in cell viability. The observed viability values in both A549 and L929 cells highlight Fe-MOF's favorable biocompatibility, which is crucial for its potential biological applications, especially in the context of biological imaging and possibly even therapeutic uses.

Furthermore, bright field images of the L929 and A549 cells treated with varying concentrations of Fe-MOF are provided in ESI Fig. S18 and S19,† respectively. These images visually demonstrate that even at higher concentrations, Fe-MOF did not cause noticeable morphological changes in the cells, further supporting its non-toxic profile. The cells appeared healthy and exhibited typical morphology, indicating that Fe-MOF did not adversely affect cellular integrity. According to the International Organization for Standardization (ISO 10993-5), which sets guidelines for the evaluation of biocompatibility, cell viability greater than 70% following treatment is not considered cytotoxic.[46]

Since both A549 and L929 cells showed viability well above this threshold, Fe-MOF can be classified as non-cytotoxic and highly biocompatible, enhancing its potential for a range of biological applications, including *in vitro* imaging and possibly *in vivo* applications.

Intracellular sensing of Fe-MOF

The sensitivity and selectivity of Fe-MOF for detecting nicotine and cotinine in A549 cells were investigated using fluorescence microscopy. To evaluate its performance, A549 cells were first incubated with 20 μg mL^{-1} of Fe-MOF for 6 hours at 37 °C, a concentration that was shown to exhibit negligible cytotoxicity in previous assays. Following this, the cells were treated separately with 5 μM, 10 μM, and 25 μM of nicotine and cotinine and incubated for an additional 3 hours. The ability of Fe-MOF to internalize into cells and its intracellular distribution was then assessed. The cellular uptake of Fe-MOF predominantly occurred *via* endocytosis, which is a well-established pathway for nano-sized materials. The spherical shape of the Fe-MOF particles was particularly favorable for this process, as it closely matches the surface curvature of the cell membrane during phagocytosis, facilitating efficient internalization.[47] Fig. 5a illustrates the intracellular distribution of Fe-MOF within the cells, showing that the nanoparticles were successfully internalized and distributed throughout the cytoplasm.

Fluorescence imaging was utilized to measure green fluorescence intensity within A549 cells. As depicted in Fig. 5e and f, cells exposed to Fe-MOF alone exhibited only faint fluorescence, suggesting limited interaction between Fe-MOF and intracellular components under these conditions. In contrast, a notable increase in fluorescence intensity was observed when cells were incubated with 25 μM of nicotine and cotinine, indicating a strong interaction of these compounds with Fe-MOF. This fluorescence enhancement implies that Fe-MOF effectively binds and accumulates both nicotine and its primary metabolite, cotinine, enabling their visualization *via* fluorescence microscopy. Similarly, treatments with lower concentrations (5 μM and 10 μM) of nicotine and cotinine are shown in Fig. S20 and S21.† This confirms Fe-MOF's capability to detect these analytes in live cells. Moreover, confocal fluorescence analysis was used to determine the mean fluorescence intensity (MFI), which revealed values of 315.356 for nicotine and 79.494 for cotinine upon interaction with Fe-MOF, as illustrated in Fig. 5c and d. These findings reinforce the potential of Fe-MOF as a sensitive tool for intracellular detection of nicotine and cotinine.

Conclusions

In summary, a novel nano-Fe-MOF was synthesized with relatively notable water stability and low cytotoxicity under solvothermal conditions. The synthesized Fe-MOF probe serves as an effective and straightforward sensing platform for detecting nicotine and cotinine in water. It features a wide response range, low detection limit, rapid response time, strong resistance to interference, and excellent recyclability. DFT calculations and UV titration experiments revealed that increased absorbance and electron transfer enhance fluorescence and induce a blue shift. The sensing applications in living cells were also investigated, demonstrating the potential of Fe-MOF as a fluorescent probe in biological sensing. This study presents a promising method for developing Fe-MOF-based sensors for the detection of nicotine and cotinine, with potential for real-world applications and broader implications in the future.

Author contributions

All authors have approved the final version of the manuscript.

Data availability

Data are available in the main article and ESI.†

Conflicts of interest

There are no conflicts to declare.

Acknowledgements

AKD, AJ, RL, and HB acknowledge INST for Ph.D. fellowships. MS and RKV thank INST for financial and infrastructural support. MS also acknowledges SERB-DST for the project EEQ/2022/000149 and CSIR EMR project 01(3064)21-EMR-II for funding. The authors also thank DST: SR/FST/CSII-07/2014

and the Institute of Eminence (IOE) grant from the University Grants Commission (UGC-Ministry of Human Resource and Development, India) for funding the single-crystal diffractometers at the Department of Chemistry, IIT Delhi.

References

1 D. Yan, Y. Lou, Y. Yang, Z. Chen, Y. Cai, Z. Guo, H. Zhan and B. Chen, *ACS Appl. Mater.*, 2019, **11**, 47253–47258.
2 I. B. Tager, *Paediatr. Respir. Rev.*, 2008, **9**, 29–38.
3 J. A. Dani and R. A. Harris, *Nat. Neurosci.*, 2005, **8**, 1465–1470.
4 N. l. Benowitz, *Annu. Rev. Pharmacol. Toxicol.*, 2009, **49**, 57–71.
5 S. Veeralingam and S. Badhulika, *ACS Appl. Nano Mater.*, 2020, **3**, 12250–12259.
6 L. M. Crosby, *Nicotine Tob. Res.*, 2024, ntae044.
7 S. A. Grando, *Nat. Rev. Cancer*, 2014, **14**, 419–429.
8 G. Maugeri, A. G. D'Amico, D. M. Rasà, V. La Cognata, S. Saccone, C. Federico, S. Cavallaro and V. D'Agata, *Toxicol. in Vitro*, 2017, **44**, 182–189.
9 D. Hoffmann, E. J. Lavoie and S. S. Hecht, *Cancer Lett.*, 1985, **26**, 67–75.
10 D. L. Ashley, W. Zhu, D. Bhandari, L. Wang, J. Feng, Y. Wang, L. Meng, B. Xia, J. M. Jarrett and C. M. Chang, *Cancer Epidemiol., Biomarkers Prev.*, 2024, **33**, 80–87.
11 P. Jacob III, M. Wilson and N. L. Benowitz, *J. Chromatogr. B:Biomed. Sci. Appl.*, 1981, **222**, 61–70.
12 H.-S. Shin, J.-G. Kim, Y.-J. Shin and S. H. Jee, *J. Chromatogr. B:Anal. Technol. Biomed. Life Sci.*, 2002, **769**, 177–183.
13 G. N. Mahoney and W. Al-Delaimy, *J. Chromatogr. B:Biomed. Sci. Appl.*, 2001, **753**, 179–187.
14 A. Marsh, B. J. Clark and K. D. Altria, *Electrophoresis*, 2004, **25**, 1270–1278.
15 K. U. Patel, D. B. Kanzariya, M. Y. Chaudhary, A. Jana, R. K. Pati, S. Das and T. K. Pal, *Inorg. Chem.*, 2024, **63**, 2352–2362.
16 A. Kuc, A. Enyashin and G. Seifert, *J. Phys. Chem. B*, 2007, **111**, 8179–8186.
17 J. Dong, D. Zhao, Y. Lu and W.-Y. Sun, *J. Mater. Chem. A*, 2019, **7**, 22744–22767.
18 T. K. Pal, D. De, S. Neogi and P. K. Bharadwaj, *Inorg. Chem. Front.*, 2015, **2**, 395–402.
19 D. Rani, K. K. Bhasin and M. Singh, *ACS Mater. Lett.*, 2019, **2**, 9–14.
20 T. K. Pal, N. Chatterjee and P. K. Bharadwaj, *Inorg. Chem.*, 2016, **55**, 1741–1747.
21 X. Guo, L. Zhou, X. Liu, G. Tan, F. Yuan, A. Nezamzadeh-Ejhieh, N. Qi, J. Liu and Y. Peng, *Colloids Surf., B*, 2023, **229**, 113455.
22 Y.-F. Guo, S. Zhao, N. Zhang, Z. Liu, P.-F. Wang, J. Zhang, Y. Xie and T.-F. Yi, *Energy Environ. Sci.*, 2024, **17**, 1725–1755.
23 J. Jia, F. Xu, Z. Long, X. Hou and M. Sepaniak, *Chem. Commun.*, 2013, **49**, 4670–4672.
24 D. Xie, Y. Ma, Y. Gu, H. Zhou, H. Zhang, G. Wang, Y. Zhang and H. Zhao, *J. Mater. Chem. A*, 2017, **5**, 23794–23804.
25 B. Liu, L. Wei, N.-n. Li, W.-P. Wu, H. Miao, Y.-Y. Wang and Q.-Z. Shi, *Cryst. Growth Des.*, 2014, **14**, 1110–1127.
26 A. Mozhdehei, L. Mercury and A. Slodsczyk, *Langmuir*, 2024, **40**, 13025–13041.
27 R. Ladhi, A. K. Dhillon and M. Singh, *Nanoscale*, 2024, **16**, 8836–8842.
28 V. Arjunan and S. Mohan, *J. Mol. Struct.*, 2008, **892**, 289–299.
29 R. K. Raji, T. Ramachandran, M. Muralidharan, R. Suriakarthick, M. Dhilip, A. Raja, K. Aravinth, S. Karthikeyan, P. Ramasamy and V. Kurapati, *J. Mater. Sci.: Mater. Electron.*, 2022, **33**, 10626–10644.
30 X. Liao, F. Wang, F. Wang, Y. Cai, Y. Yao, B.-T. Teng, Q. Hao and L. Shuxiang, *Appl. Catal., B*, 2019, **259**, 118064.
31 Q. Xie, Y. Li, Z. Lv, H. Zhou, X. Yang, J. Chen and H. Guo, *Sci. Rep.*, 2017, **7**, 3316.
32 L. H. T. Nguyen, S. T. Navale, D. H. Yang, H. T. T. Nguyen, T. B. Phan, J.-Y. Kim, A. Mirzaei, T. L. H. Doan, S. S. Kim and H. W. Kim, *Sens. Actuators, B*, 2023, **388**, 133799.
33 F. Khosravi, M. Gholinejad, J. M. Sansano and R. Luque, *Appl. Organomet. Chem.*, 2022, **36**, e6749.
34 A. Joshi, A. Gaur, P. Sood and M. Singh, *Inorg. Chem.*, 2021, **60**, 12685–12690.
35 S. B. Chanu, M. K. Raza, D. Musib, M. Pal, M. Pal and M. Roy, *Chem. Lett.*, 2020, **49**, 724–727.
36 L. Hanna, P. Kucheryavy, C. Liu, X. Zhang and J. V. Lockard, *J. Phys. Chem. C*, 2017, **121**, 13570–13576.
37 J. Stahl and B. König, *Green Chem.*, 2024, **26**, 3058–3071.
38 L. Yang, C. Lian, X. Li, Y. Han, L. Yang, T. Cai and C. Shao, *ACS Appl. Mater. Interfaces*, 2017, **9**, 17208–17217.
39 R. Ladhi, D. Rani and M. Singh, *New J. Chem.*, 2023, **47**, 9714–9720.
40 B.-L. Hou, D. Tian, J. Liu, L.-Z. Dong, S.-L. Li, D.-S. Li and Y.-Q. Lan, *Inorg. Chem.*, 2016, **55**, 10580–10586.
41 T. Gao, L. Gao, J. Zhang, W. Zhou, Z. Zhang, X. Niu and T. Hu, *J. Lumin.*, 2021, **231**, 117798.
42 Y.-W. Zhao, L.-E. Guo, F.-Q. Zhang, J. Yao and X.-M. Zhang, *ACS Appl. Mater. Interfaces*, 2021, **13**, 20821–20829.
43 C. Yang and B. Yan, *Inorg. Chem.*, 2023, **62**, 20458–20466.
44 T. Gong, P. Li, Q. Sui, J. Chen, J. Xu and E.-Q. Gao, *J. Mater. Chem. A*, 2018, **6**, 9236–9244.
45 S. Guria, A. Ghosh, K. Manna, A. Pal, A. Adhikary and S. Adhikari, *Dyes Pigm.*, 2019, **168**, 111–122.
46 I. J. G. Standard, *International Organization for Standardization*, 2009, **92**, 527–537.
47 D. Paul, S. Achouri, Y.-Z. Yoon, J. Herre, C. E. Bryant and P. Cicuta, *Biophys. J.*, 2013, **105**, 1143–1150.

